

RANS Simulation of the Transitional Flow Around Airfoils at Low Reynolds Numbers for Steady and Unsteady Onset Conditions

Jan Windte, Rolf Radespiel and Ulrich Scholz

Institute of Fluid Mechanics,

Technical University Braunschweig, Germany

Tel./Fax: +49 531 391 2978/5952

j.windte@tu-braunschweig.de

Bernhard Eisfeld

Institute of Aerodynamics and Flow Technology,

German Aerospace Center, Germany

Tel./Fax: +49 531 295 3305/2320

bernhard.eisfeld@dlr.de

ABSTRACT

RANS computations around airfoils are presented for flows where transition takes place across a laminar separation bubble. Transition locations are found employing the e^N -method and a linear stability solver that uses the velocity and temperature profiles from the RANS-solution. Hereby, the known e^N -method is applied for the flows with steady onset conditions, whereas a new temporal scheme for the e^N -method is used for the flow around a plunging airfoil. Obtained numerical results are compared to hotwire-, pressure- and PIV-measurements of laminar separation bubbles.

1 INTRODUCTION

The aerodynamics of low-speed low-Reynolds-number flows over airfoils and wings has been studied for decades in experimental and numerical works. However, the research was often of an academic nature since there were few technical applications. One exception was the design of model airplanes for which a rich experimental data base grew over the years. Here the pioneering work of F. Schmitz [1] is mentioned, and much work was later performed by researchers at Stuttgart University, Germany [2], [3]. More recently, M. Selig and co-workers continued to develop advanced aerodynamic design methodologies for model airplane airfoils and performed a large amount of measurements [4], [5]. The subject of low-Reynolds number flows does receive more attention presently as advances in the field of micro system technologies enable the development of Micro Aerial Vehicles (MAV) with a broad variety of applications. In this context it is useful to view the range of existing and future unmanned aerial vehicles by using the Reynolds number as the flow parameter, see **Tab. 1**. Dimensional analysis states that the Reynolds number is the governing parameter that determines lift and drag of a given geometrical shape and a fixed disturbance level of the incoming freestream flow.

	MAV long term	MAV medium term	Current MAV	Small drones	Drones
Mass	1g	10g	100g	5kg	50kg
Reynolds number	$10^3 - 10^4$	$10^4 - 5 \cdot 10^4$	$5 \cdot 10^4 - 2 \cdot 10^5$	$2 \cdot 10^5 - 5 \cdot 10^5$	$5 \cdot 10^5 - 2 \cdot 10^6$
Wing configuration	Flapping	Fixed, rotary, flapping	Fixed, rotary	Fixed	Fixed

Tab. 1: Range of airfoil Reynolds numbers relative to Micro Air Vehicle weight

Paper presented at the RTO AVT Specialists' Meeting on "Enhancement of NATO Military Flight Vehicle Performance by Management of Interacting Boundary Layer Transition and Separation", held in Prague, Czech Republic, 4-7 October 2004, and published in RTO-MP-AVT-111.

Report Documentation Page			Form Approved OMB No. 0704-0188					
<p>Public reporting burden for the collection of information is estimated to average 1 hour per response, including the time for reviewing instructions, searching existing data sources, gathering and maintaining the data needed, and completing and reviewing the collection of information. Send comments regarding this burden estimate or any other aspect of this collection of information, including suggestions for reducing this burden, to Washington Headquarters Services, Directorate for Information Operations and Reports, 1215 Jefferson Davis Highway, Suite 1204, Arlington VA 22202-4302. Respondents should be aware that notwithstanding any other provision of law, no person shall be subject to a penalty for failing to comply with a collection of information if it does not display a currently valid OMB control number.</p>								
1. REPORT DATE 01 OCT 2004	2. REPORT TYPE N/A	3. DATES COVERED -						
RANS Simulation of the Transitional Flow Around Airfoils at Low Reynolds Numbers for Steady and Unsteady Onset Conditions			5a. CONTRACT NUMBER					
			5b. GRANT NUMBER					
			5c. PROGRAM ELEMENT NUMBER					
6. AUTHOR(S)			5d. PROJECT NUMBER					
			5e. TASK NUMBER					
			5f. WORK UNIT NUMBER					
7. PERFORMING ORGANIZATION NAME(S) AND ADDRESS(ES) Institute of Fluid Mechanics, Technical University Braunschweig, Germany			8. PERFORMING ORGANIZATION REPORT NUMBER					
9. SPONSORING/MONITORING AGENCY NAME(S) AND ADDRESS(ES)			10. SPONSOR/MONITOR'S ACRONYM(S)					
			11. SPONSOR/MONITOR'S REPORT NUMBER(S)					
12. DISTRIBUTION/AVAILABILITY STATEMENT Approved for public release, distribution unlimited								
13. SUPPLEMENTARY NOTES See also ADM201868, RTO-MP-AVT-111 Enhancement of NATO Military Flight Vehicle Performance by Management of Interacting Boundary Layer Transition and Separation (L'amélioration des performances des véhicules aériens militaires de l'OTAN par la gestion de l'interaction entre la transition et le décollement de la couche limite),, The original document contains color images.								
14. ABSTRACT								
15. SUBJECT TERMS								
16. SECURITY CLASSIFICATION OF: <table border="1" style="width: 100%; border-collapse: collapse;"> <tr> <td style="width: 33%; padding: 2px;">a. REPORT unclassified</td> <td style="width: 33%; padding: 2px;">b. ABSTRACT unclassified</td> <td style="width: 33%; padding: 2px;">c. THIS PAGE unclassified</td> </tr> </table>			a. REPORT unclassified	b. ABSTRACT unclassified	c. THIS PAGE unclassified	17. LIMITATION OF ABSTRACT UU	18. NUMBER OF PAGES 20	19a. NAME OF RESPONSIBLE PERSON
a. REPORT unclassified	b. ABSTRACT unclassified	c. THIS PAGE unclassified						

RANS Simulation of the Transitional Flow Around Airfoils at Low Reynolds Numbers for Steady and Unsteady Onset Conditions

Very small aerial vehicles foreseen in the long term will most likely exhibit a laminar flow. At larger Reynolds numbers, mixed laminar and turbulent flows occur with transition in between. Moreover, it turns out that aerodynamic designs for Reynolds numbers in the range between 10^4 and 10^6 face a flow phenomenon called laminar separation bubble (LSB). The LSB is a flow where a laminar separation takes place that is in most cases caused by an adverse pressure gradient along the smooth aerodynamic surface. Small disturbances present in the laminar flow are strongly amplified in the shear layer of the separated flow and rapid transition to turbulence takes place. The turbulence, in turn, creates a large momentum transport normal to the shear layer so that the flow reattaches to the surface and a closed bubble is formed in the time-averaged mean.

Laminar separation bubbles can have large, adverse aerodynamic effects. Usually, they create additional drag as they displace the outer inviscid flow. This results in reduced suction over the forward portion of airfoils and wings and decreases pressure recovery in rear parts, so the additional drag is mostly pressure drag. The increase of pressure drag depends on the size of the LSB, in particular on its thickness in the normal-wall direction. A more dramatic effect occurs if the transition process in the separated shear layer is relatively slow and the adverse pressure gradient is strong. Then turbulent momentum transport is not sufficient to close the bubble and a large separation occurs that extends right to the trailing edge. This causes a sudden loss of lift and a strong increase of drag along with significant hysteresis effects of force coefficients with varying angle of attack. Note that the break up of LSBs may be experienced over a broad range of Reynolds numbers.

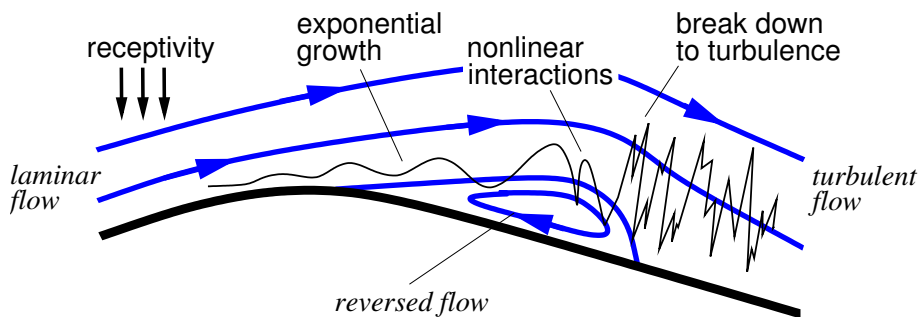


Fig. 1: Instability and transition in a laminar separation bubble, with a sketch of time-averaged streamlines

The principal flow behaviour of a laminar separation bubble is sketched in Fig. 1. External distortions, for example acoustic waves or free stream turbulence, generate small, harmonic waves within the laminar boundary layer upstream of the separation. The behaviour of the waves of the laminar boundary layer can be described by linear stability theory (LST) within a certain spatial region: unstable waves grow exponentially while travelling downstream. This linear process constitutes the second stage of transition. In the third stage of transition the distortions become so large that saturation occurs and secondary instabilities can grow on the distorted boundary layer flow: This behaviour is denoted with nonlinear interactions. Finally, the number of spatial and temporal modes grows rapidly and the ordered laminar structures break down to turbulence.

Transition in 2D laminar separation bubbles is dominated by the behaviour of the primary 2D disturbances within the laminar boundary layer (called Tollmien-Schlichting modes), according to the research of Rist, Würz and Wagner ([6], [7], [8]). Initial 3D-disturbances are also amplified but numerical and experimental evidence indicates that they do not govern the transition process and its location.

2 FLOW MODELLING FOR ENGINEERING COMPUTATIONS

Aerodynamic design and analysis tools used for flows with laminar separation bubbles are presently restricted to 2D steady flows [9] and they are rather not reliable in their predictions of the break-up process of LSBs. For the future design of MAV's more general analysis tools are sought, which can be applied to 2D airfoils as well as 3D flows over more complex configurations. Direct Numerical Simulation (DNS) of the flow during aerodynamic design cycles is not feasible because of the extreme demands on computational resources



RANS Simulation of the Transitional Flow Around Airfoils at Low Reynolds Numbers for Steady and Unsteady Onset Conditions

associated with this approach. This paper therefore presents the current status in modelling and computation of low-Reynolds number flows with laminar separation bubbles using the Reynolds-averaged Navier-Stokes equations. This engineering approach is expected to complement the existing approximate methods in the near future. The main issues using this approach are the modelling of the transition laminar turbulent as well as accurate turbulence modelling.

2.1 Transition Modelling

2.1.1 Linear Stability Theory

For 2D flows the Linear Stability Theory uses a coordinate system (x,z) that is aligned with the local edge velocity of the undisturbed laminar mean flow such that x is streamwise and z is wall normal. The baseflow at a given x position is represented by (U,0), i.e. parallel 2D flow. The perturbation stream function representing a single Tollmien-Schlichting wave is then assumed to be of the form:

$$\Psi(x, z, t) = \hat{\phi}(z) e^{i\alpha(x - \omega t)} \quad (1)$$

The components of the perturbation velocity can then be expressed as:

$$u' = \frac{\partial \Psi}{\partial z} = \hat{\phi}'(z) e^{i(\alpha x - \omega t)} + cc, \quad (2)$$

$$w' = \frac{\partial \Psi}{\partial x} = -i\alpha \hat{\phi}(z) e^{i(\alpha x - \omega t)} + cc. \quad (3)$$

Herein, α and ω are in general complex,

$$\alpha = \alpha_r + i\alpha_i, \quad (4)$$

$$\omega = \omega_r + i\omega_i, \quad (5)$$

with α_r being the wave number (wavelenght $\lambda = 2\pi/\alpha_r$), ω_r the circular frequency and α_i , ω_i amplification rates. It can then be distinguished between a spatial and a temporal theory: In the spatial theory ω is real, and amplification rates $\alpha_i < 0$ denote spatial amplified disturbances in flow direction, while in the temporal theory α is real and amplifications in time are given for amplification rates $\omega_i > 0$ and given positions x.

Using the spatial theory and introducing the perturbation velocities, eq. 2 and 3, into the Navier-Stokes equations, one can obtain the Orr-Sommerfeld equation for the amplitude $\hat{\phi}$:

$$\hat{\phi}''' - 2\alpha^2 \hat{\phi}'' + \alpha^4 \hat{\phi} = iRe[(\alpha U - \omega)(\hat{\phi}'' - \alpha^2 \hat{\phi}) - \alpha U'' \hat{\phi}]. \quad (6)$$

Using homogenous boundary conditions for the perturbations at the wall and for large values of y, the problem of stability is now reduced to an eigenvalue problem of eq. 6, assuming that the mean flow, Reynolds number and circular frequency ω are given. Then, the solution yields the most unstable complex eigenvalue $\alpha = \alpha_r + i\alpha_i$.

2.1.2 Transition Prediction for Unsteady Flow with the e^N -Method

A quite successful method for transition predictions was derived from observations, that the location of the final transition phase (break down) is in many cases dominated by the behaviour of the primary instabilities with exponential growth. It has been found that the point where the boundary layer becomes fully turbulent correlates strongly with a certain amplification factor of the most unstable primary wave that is calculated from the point of neutral stability up to the location with fully turbulent flow. These findings constitute the so called e^N -method.

The assumptions needed to apply the method to the problem of predicting transition of LSBs include:

- Initial and external disturbances of the laminar boundary layer are small. These are the surface roughness, external turbulence, acoustic disturbances, noise, and probably others.

RANS Simulation of the Transitional Flow Around Airfoils at Low Reynolds Numbers for Steady and Unsteady Onset Conditions



- The location of the final transition phase (break down) is governed by the behaviour of primary 2D-waves (Tollmien-Schlichting waves).
- The laminar boundary layer is thin and grows slowly with x .

The last assumptions may appear questionable, at first sight. However, extensive numerical experience from numerical stability computations and comparisons with the results of DNS by U. Rist and his co-workers indicates that the assumption of parallel flow needed for the LST formulated above is valid. That is, the growth rates of primary instabilities computed by LST compares very well with the rates predicted by well resolved DNS [10], [11].

In the spatial theory, the overall amplification factor $A(x)/A_0$ of the perturbation amplitude A is built by an integration of the local amplification rates α_i :

$$\frac{A(x)}{A_0} = e^{-\int_{x_0}^x \alpha_i dx}. \quad (7)$$

This integration is done for a fixed number of values for the circular frequency ω . The so called N-factor is then obtained by taking the maximum value of the amplitude exponent

$$N = \max \left(- \int_{x_0}^x \alpha_i(x, \omega) dx \right), \quad (8)$$

and thus forms an envelope over the investigated modes. This is shown in **Fig. 2** for the example of the flow over a flat plate.

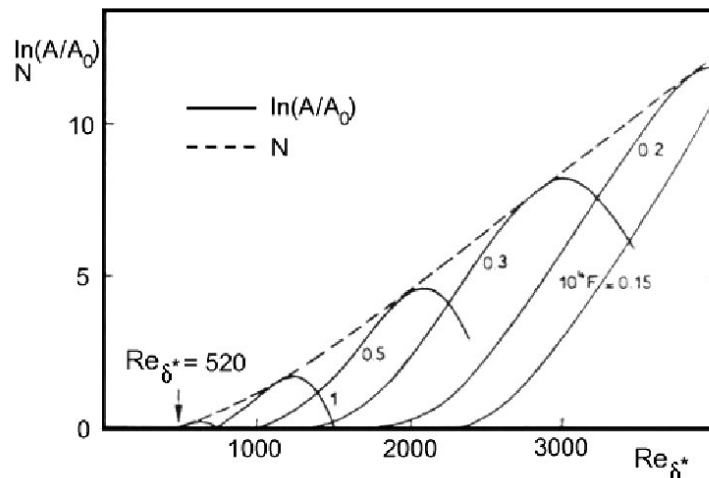


Fig. 2: Application for flat plate, from D.Arnal [12]

The energy of a wave propagates with the group velocity

$$v_g = \frac{\partial \omega_r}{\partial \alpha}, \quad (9)$$

which gives the link between the spatial and temporal amplification rates, known as Gaster transformation:

$$\omega_i = -\alpha_i v_g. \quad (10)$$

Then, while the energy of a mode is convected downstream to a position $\tilde{x} = x + v_g \Delta t$, its perturbation amplitude is amplified by

$$\Delta n = \ln \frac{A(\tilde{x})}{A(x)} = \int_t^{t+\Delta t} \omega_t(x) dt \quad (11)$$

This can be used to calculate amplitude exponents for unsteady flows using a simple temporal integration scheme. For the new position \tilde{x} and for a single mode at the time $t + \Delta t$ this yields:

$$n(\tilde{x}) = n(x) + \Delta n(x). \quad (12)$$

The N-Factor is than again obtained by taking the maximum value of the amplitude exponents n of the single modes.

The transition location is found by assuming a critical N-factor at which transition is completed and comparing it to the calculated N-Factor distribution. For external flows over airfoils and wings in wind tunnels the main factor influencing the critical N-factor is the free-stream turbulence level of the test section. An empirical correlation between the turbulence level Tu and the critical N-factor N_{crit} is given by Mack [13]:

$$N_{crit} = -8.43 - 2.4 \ln(Tu) \quad (13)$$

2.1.3 Approximate Envelope Method for Steady Flow

Exact solutions of the two-dimensional boundary layer equations for laminar flow can be obtained by solving the Falkner-Skan equation

$$f''' + f'' + \beta_h(1 - f'^2) = 0, \quad (14)$$

where the non-dimensional streamfunction $f(\eta)$ depends only on the wall-normal coordinate. The solution describes the flow past a wedge with the wedge angle equal to $\pi\beta_h$ and consist of self-similar velocity profiles. These were studied in detail by D.R. Hartree, therefore the parameter β_h is referred to as Hartree-parameter and the corresponding velocity profiles as Hartree profiles. For every Hartree profile a distinct shape parameter H can be affiliated.

Each Hartree profile can now be analysed similar to the flat plate as shown in **Fig. 2**, which is the special case of the flow past a wedge with an angle of 0° ($\beta_h = 0$). This yields envelope curves similar to the one in **Fig. 2**, in dependence of the shape parameter H . These curves can be approximated by linear functions. These functions are governed by two parameters, one for the intersection with the abscissa and one for the gradient. Polynomials may be defined that yield numerical values of these parameters and these polynomials are meant when referring to “the” envelope. The envelope used for the calculations in the present paper has been created by Würz [6] using tables calculated by Arnal. In order to apply this envelope for the flow around an airfoil it is assumed that the velocity profiles of the airfoil boundary layer are similar to the Falkner-Skan flows with the same shape parameter H . Therefore, they are assumed to exhibit the same stability behaviour.

2.2 Turbulence Modelling

Turbulence modelling for engineering applications is usually based on the Reynolds averaged Navier-Stokes equations. In this approach the contribution of turbulence to the mean momentum is accounted for by the divergence of the so-called Reynolds stress tensor, which has to be modelled in terms of mean flow quantities.

Most models rely on the Boussinesq hypothesis, namely that the Reynolds stress tensor is proportional to the mean (traceless) shear tensor, i. e.

$$\rho R_{ij} = -\mu_t \left(\frac{\partial U_i}{\partial x_j} + \frac{\partial U_j}{\partial x_i} - \frac{2}{3} \frac{\partial U_k}{\partial x_k} \delta_{ij} \right) + \frac{2}{3} \rho k \delta_{ij}, \quad (15)$$

where U_i are the mean velocity components and k is the kinetic turbulence energy. The proportionality coefficient μ_t is the eddy viscosity and must be provided by the respective model.

In algebraic turbulence models, like that of Baldwin and Lomax [14], the eddy viscosity is provided by some algebraic relation, often based on Prandtl's mixing length concept.

Improvements are achieved using one or two-equation models. The one-equation model of Spalart-Allmaras [15] uses a transport equation for a value strongly related to the turbulent viscosity with rather heuristic modelling of turbulence diffusion, production and destruction. However, this model is numerically very robust and therefore widely used for applications. Two-equation models exploit transport equations for the kinetic turbulence energy k and some length scale of the turbulent eddies, e. g. ε or ω . A model of this class that is becoming increasingly popular is the SST model of Menter [16], which reads

$$\frac{\partial(\rho k)}{\partial t} + \frac{\partial}{\partial x_j}(\rho k U_j) = \frac{\partial}{\partial x_j} \left[(\mu + \sigma_k \mu_t) \frac{\partial k}{\partial x_j} \right] - \rho R_{ij} \frac{\partial U_i}{\partial x_j} - \beta^* \rho k \omega, \quad (16)$$

$$\begin{aligned} \frac{\partial(\rho \omega)}{\partial t} + \frac{\partial}{\partial x_j}(\rho \omega U_j) &= \frac{\partial}{\partial x_j} \left[(\mu + \sigma_\omega \mu_t) \frac{\partial \omega}{\partial x_j} \right] + \sigma_d \frac{\rho}{\omega} \max \left(\frac{\partial k}{\partial x_j} \frac{\partial \omega}{\partial x_j}; 10^{-20} \right) \\ &\quad - \gamma \frac{\rho}{\mu_t} \rho R_{ij} \frac{\partial U_i}{\partial x_j} - \beta \rho \omega^2. \end{aligned} \quad (17)$$

This model combines the advantages of k - ε and k - ω models by gradually changing the closure coefficients β , β^* , γ , σ_d , σ_k and σ_ω via a blending function F_1 . Additionally the model has been sensitized to predict separation more reliably by defining the eddy viscosity as

$$\mu_t = \frac{a_1 \rho k}{\max(a_1 \omega; F_2 \Omega)}, \quad (18)$$

where Ω is the absolute value of the vorticity and F_2 is a function depending on the wall distance. Nevertheless all these models suffer from the weaknesses of the Boussinesq assumption (15).

This drawback is overcome by solving the transport equations for the individual Reynolds stress components R_{ij} , which read

$$\frac{\partial(\rho R_{ij})}{\partial t} + \frac{\partial}{\partial x_k}(\rho R_{ij} U_k) = \rho P_{ij} + \rho D_{ij} - \rho \varepsilon_{ij} + \rho \Pi_{ij}. \quad (19)$$

In contrast to two-equation models, in this approach the production term $\rho P_{ij} = -\rho R_{ik} \frac{\partial U_j}{\partial x_k} - \rho R_{jk} \frac{\partial U_i}{\partial x_k}$ is exact, while the diffusion term ρD_{ij} , the destruction term $\rho \varepsilon_{ij}$ and, in addition, the redistribution term $\rho \Pi_{ij}$ need to be modelled. In this context simple gradient diffusion is assumed, i. e. $\rho D_{ij} = \frac{\partial}{\partial x_k} \left[(\mu + C_s \rho k^2 / \varepsilon) \frac{\partial R_{ij}}{\partial x_k} \right]$, while for the destruction term it is common practice to assume isotropy, i. e. $\varepsilon_{ij} = \frac{2}{3} \varepsilon \delta_{ij}$. Like in two-equation models, ε (or ω) must be provided by an additional length scale equation.

A redistribution model that performs very well in homogenous turbulence is the SSG model [17], reading

$$\begin{aligned} \Pi_{ij} &= - \left(C_1^{(0)} \varepsilon + \frac{1}{2} C_1^{(1)} P_{kk} \right) b_{ij} + C_2 \varepsilon \left(b_{ik} k_{kj} - \frac{1}{3} b_{mn} b_{mn} \delta_{ij} \right) + \left(C_3 - C_3^* \sqrt{b_{mn} b_{mn}} \right) k S_{ij} \\ &\quad + C_4 k \left(b_{ik} S_{jk} + b_{jk} S_{ik} - \frac{2}{3} b_{mn} S_{mn} \delta_{ij} \right) - C_5 k (b_{ik} W_{kj} - W_{ik} b_{kj}) \end{aligned} \quad (20)$$

In this equation $b_{ij} = R_{ij}/2k - \delta_{ij}/3$ is called the anisotropy tensor, and S_{ij} and W_{ij} represent the shear and the rotation tensors, respectively. For the wall bounded flows investigated here the model has been combined with the somewhat simpler stress- ω model of Wilcox [18] near walls by gradually changing the coefficients C_i via the blending function F_1 of the SST model [19]. Equation (17) is used for providing the length scale.

3 NUMERICAL METHODS

3.1 Navier Stokes Code FLOWer

The Navier-Stokes solver FLOWer [20] uses a block-structured computational domain around the aerodynamic configuration. The flow equations are discretised based on the finite-volume approach, either with the cell-vertex or the cell-centred formulations. Various options are implemented for treating the convective fluxes. These are central schemes with scalar or matrix valued dissipation and upwind schemes as well. Integration in time is performed by explicit multistage schemes. Implicit residual averaging, multigrid and local time steps improve convergence for steady-state flow computation. Time-accurate computations are supported by using the dual time stepping approach. Both convergence and accuracy of low-speed flow simulations are enhanced by preconditioning. The code is optimised for vector computers. Parallel computations are based on MPI and the use of a high-level communication library. A variety of turbulence models is implemented into FLOWer. These include algebraic eddy-viscosity models, one- and two equation models, algebraic stress models and Reynolds stress models. Among these the one-equation model of Spalart-Allmaras and the $k - \omega$ model of Wilcox are standard options, but their variants SST, LEA, EARSM have shown improved results for specific applications, particularly with turbulent flow separations.

3.2 Linear Stability Equations Solver Coast3

The numerical method used for determining local amplification of disturbances is more general compared to the stability theory based on the Orr-Sommerfeld equation as presented in chapter 2.1. Coast3 treats laminar, compressible boundary layers [21]. The boundary layer is assumed to be a parallel flow. The harmonic wave ansatz is applied to the variables u, v, w, p, T . It results in a system of five linear differential equations with an option to include curvature effects. Coast3 solves the eigenvalue problem for the complex eigenvalue ω , where the wave numbers α and β (for 3D-Cases) are prescribed by the user. Hence the temporal stability problem is solved. The system of differential equations is discretised with symmetrical second-order differences. This yields a $5n$ -dimensional complex band matrix where n is the number of grid points in wall-normal direction. The numerical eigenvalue computation is accomplished with a generalised inverse Rayleigh iteration [22] that takes into account the banded structure of the algebraic problem. The code provides efficient searching strategies that can be used to find the range of unstable modes for a given flow problem. A data base method to find the range of amplified spanwise wave numbers is offered as well. Also an option for boundary layer computations for a given pressure distribution is available.

4 IMPLEMENTATION ISSUES

4.1 Extraction of Boundary Layer Parameters

In order to calculate N-factor distributions with the approximate envelope method as well as the linear stability solver, several integral boundary layer parameters have to be extracted from the Navier-Stokes solution. Therefore, the boundary layer edge has to be detected first. As the pressure can be assumed to be constant normal to the boundary layer, the boundary layer edge velocity U_e can be calculated from the wall pressure, p_w , using the compressible Bernoulli equation:

$$U_e = \sqrt{U_\infty^2 - \frac{2\kappa}{\kappa-1} \frac{p_\infty}{p_w} \left[\left(\frac{p_w}{p_\infty} \right)^{\frac{\kappa-1}{\kappa}} - 1 \right]}. \quad (21)$$

Then, the boundary layer thickness δ is found at the point in wall-normal direction where a specified fraction $U = c \cdot U_e$ of the edge velocity is reached, with $c = 0.99$ as a typical value. If U is not reached, then the point with the maximum velocity is taken instead. These criterions do not perform well close to the leading stagnation point. Therefore, all points with a surface pressure coefficient c_p of more than 95 percent of

RANS Simulation of the Transitional Flow Around Airfoils at Low Reynolds Numbers for Steady and Unsteady Onset Conditions

the stagnation value are excluded. This can be safely done because disturbances are damped in this region anyway.

As the wall boundary layer has, in contrast to the parallel flow assumption of the boundary layer theory, a small velocity component v normal to the wall, the absolute velocity is used for U_e here,

$$U_e = \sqrt{u^2 + v^2}, \quad (22)$$

while the wall tangential velocity component is used for U to calculate the boundary layer parameters:

$$U = U_{tan}. \quad (23)$$

The displacement thickness δ^* and the momentum loss thickness θ can be determined by integration from the wall to the boundary layer edge:

$$\delta^* = \int_0^\delta \left(1 - \frac{U}{U_e}\right) dy ; \quad \theta = \int_0^\delta \frac{U}{U_e} \left(1 - \frac{U}{U_e}\right) dy \quad (24)$$

Using the above values for δ^* and θ , the shape parameter and the Reynolds number based on θ , the velocity U_e and the viscosity ν_e at the boundary layer edge can be determined:

$$H = \frac{\delta^*}{\theta} , \quad Re_\theta = \frac{U_e \theta}{\nu_e} . \quad (25)$$

4.2 Treatment of Stability Data Close to the Numerical Transition Location

The numerical update of the transition location requires special attention: Switching on the source terms of the turbulence model at the predicted transition location will numerically affect the laminar, boundary layer just upstream of that point, by the inherent discretisation errors of the numerical scheme. This numerical error can have adverse effects on the further transition prediction result if no adequate treatment is introduced into the transition location update. In our experience, for the LST-solver as well as the approximative envelope methods, this is mainly an issue in attached flows. Also, separated flows are effected if turbulence models are used which react abruptly to their activation, like algebraic turbulence models. We have therefore developed a new method for extracting reliable transition location estimates from stability results based on RANS mean flow data. The method is based on streamwise linear extrapolation of N-factors from flow regions with reliable laminar mean flow into the transitional or even turbulent locations. The method searches for non-physical gradients of the N-factor or local maxima that are caused by the numerical discretisation errors close to transition in order to find the extrapolation region in an automated way. A sample using the approximative envelope method is shown in **Fig. 3**. The result is taken from an airfoil computation where transition takes place above a LSB. Here, the investigation of the turbulent region behind as well as the influenced region ahead of the transition location results in a strong, nonphysical increase of the N-Factor, which is overcome by the linear extrapolation. Without the extrapolation, not only the transition location would be false, but also oscillations could occur, as sometimes the local maximum ahead of the strong increase of the N-Factor is detected at transition location. Much stronger oscillations can appear using the linear stability solver in attached flows, as shown in **Fig. 4**. Here, with increasing time it can happen that no transition location is found at all. As the transition location is then set to the trailing edge, one obtains a strongly amplified laminar region and thus the transition location moves to the previous position. The linear extrapolation method can therefore be used to avoid these unphysical oscillations. Note that the e^N -method itself is an extrapolation technique of linear stability results to the transition point upstream of which nonlinear effects dominate in reality. Therefore, a local extrapolation of N-factors is an acceptable modification of the overall e^N -method. Finally, under-relaxation in the iterative update of the numerical transition location may be used in order to damp oscillations in the iterative transition location update.

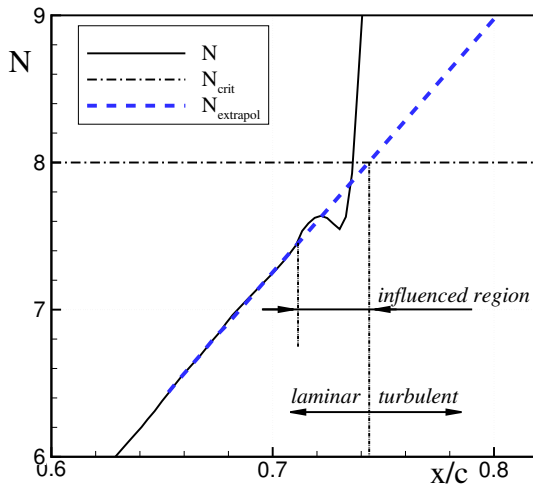


Fig. 3: N-Factor distribution for separated flow using the approximative envelope method

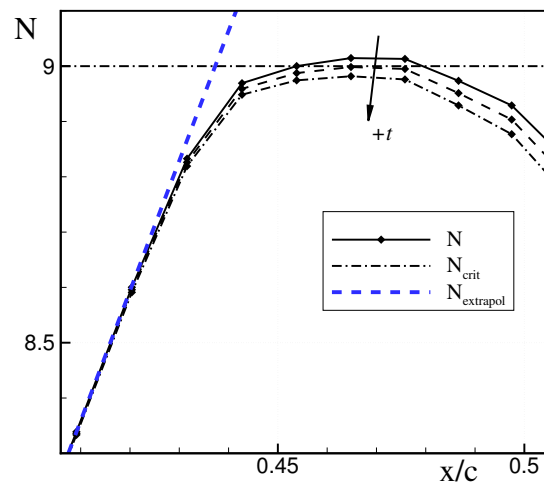


Fig. 4: N-Factor distribution for attached flow using the linear stability solver

4.3 Transition Prediction Procedure Using the Linear Stability Solver

4.3.1 Approach for Steady Flows

For the calculation of steady state flows the linear stability solver is used in usual ways. First, the frequency range of amplified modes is estimated. Therefore all eigenvalues at an initial station are searched. Then, the mode with the most amplified eigenvalue at this station is tracked up- and downstream until it is not amplified anymore. At these two positions, the modes with the highest and lowest frequency that are still amplified are determined. Second, a N-factor analysis is performed in the previously determined frequency range for a number of fixed frequencies. For all these given frequencies F , the most amplified modes are tracked up- and downstream until they are damped. Their temporal amplification rates are calculated in this region and transformed in spatial ones using the Gaster transformation. These are then integrated to N-factor distributions in the amplified region for every frequency. The envelope over all these N-factor distributions then yields the N-factor curve which is used to determine the transition location by comparison with a critical N-factor.

4.3.2 Approach for Unsteady Flows

For a given frequency multiple modes with different wavenumbers and amplification rates may be found by the numerical method. As the N-factor distribution for a given frequency is now computed with a time-dependant scheme, it has to be made sure that at every timestep the same modes are analysed. This is not guaranteed with the above approach for steady flows, which is why it is now used in a modified way. As the mean flow changes with time, also the frequency range of amplified modes changes. Accordingly, the investigated range of frequencies has to be adapted during an unsteady calculation. For the present computations, this is circumvented by selecting a fixed frequency range and checking afterwards if the frequencies that were relevant for the transition were investigated at all times. The N-Factor analysis is then performed once for every mode, using the modes wavelengths and amplification rates from the last timestep as initial values for the solver to make sure that the same mode is investigated again. As new amplified modes can form in unsteady flows, these are searched after every timestep along the airfoil for the investigated frequencies. Also, modes that are damped to the point where the amplitude exponent is zero over the whole airfoil are identified and deleted.

RANS Simulation of the Transitional Flow Around Airfoils at Low Reynolds Numbers for Steady and Unsteady Onset Conditions

5 NUMERICAL FLOW COMPUTATIONS

Steady state flow solutions are often not obtained for flows with LBS's, even with Reynolds averaging of the flow equations. As a consequence, the RANS solver is run in its time-accurate mode using the dual time-stepping approach, even for steady onset conditions. As a rule of thumb we use a time step length of $\Delta t \approx 0.01$, where the time is made non-dimensional by using the onset flow velocity and the chord length. **Figure 5** indicates that this time is sufficiently small to resolve the main viscous boundary layer interactions. For unsteady onset conditions there remains a very small influence on the temporal distribution of the transition location, as seen in **Fig. 6**. As the influence on the distribution of the force coefficients is negligible, no shorter timestep than $\Delta t \approx 0.01$ was chosen to minimise the computational time.

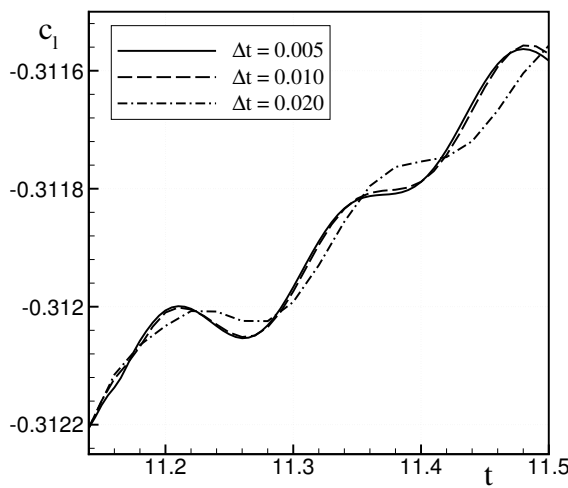


Fig. 5: Variation of timestep length for steady onset conditions at $Re = 1.2 \cdot 10^6$

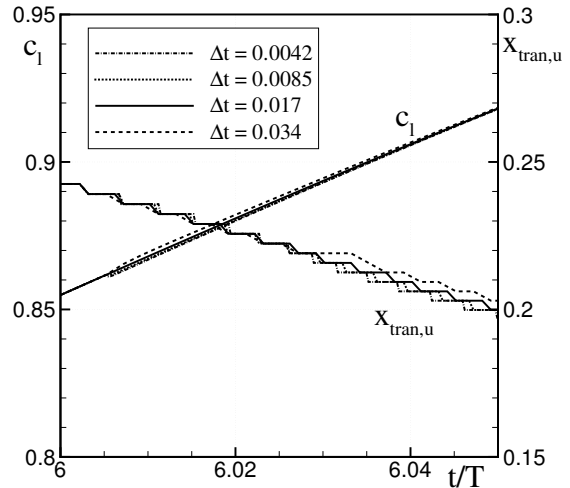


Fig. 6: Variation of timestep length for unsteady onset conditions at $Re = 60000$

5.1 Steady Onset Conditions

5.1.1 Flow Computations of XIS40MOD Airfoil

Numerical computations of the research airfoil XIS40MOD are chosen because there exists detailed experimental data of Würz [6] from a low-disturbance wind tunnel. The measured data include pressure distributions and boundary-layer flow velocities measured with a hot wire (mean flow and flow disturbances). The airfoil is specifically designed to produce a large laminar separation bubble on its upper surface (see **Fig. 7**). The computational mesh shown has 528 cells in surface-tangential direction whereas normal to the surface 96 cells are used. This is the standard mesh. The mesh points are clustered around the leading edge and around the expected LBS. About 40 out of 96 wall-normal cells are located in the laminar boundary layer (not shown here). More refined meshes have been generated in order to obtain grid convergence. The fine mesh has 1056x192 cells and a super-fine mesh with 2112x384 cells was also used. The flow conditions are chosen as $Re = 1.2 \cdot 10^6$ and $\alpha = -3^\circ$, according to the experiment. The first round of computations is performed using a fixed transition location at $x/l = 0.76$ on the upper airfoil surface in order to address the effect of spatial 0 errors on the numerical solutions. The results are displayed in **Fig. 8** and **Fig. 9**. The computations are performed with the SST turbulence model. The pressure distribution and skin friction are well resolved in the region of attached flow using the 528x96 mesh. However, it takes a grid of around 1056x192 points in order to capture the laminar separation accurately. The grid-converged computation exhibits a pressure rise in the rear part of the bubble that is not as steep as in the experimental data. Also, the wall shear stress downstream of reattachment is significantly smaller in the computation compared with the measurement.

The next computations are used to investigate the effect of varying the turbulence model. These computations are performed on the 528x96 grid. The results of the algebraic model of Baldwin and Lomax are

RANS Simulation of the Transitional Flow Around Airfoils at Low Reynolds Numbers for Steady and Unsteady Onset Conditions

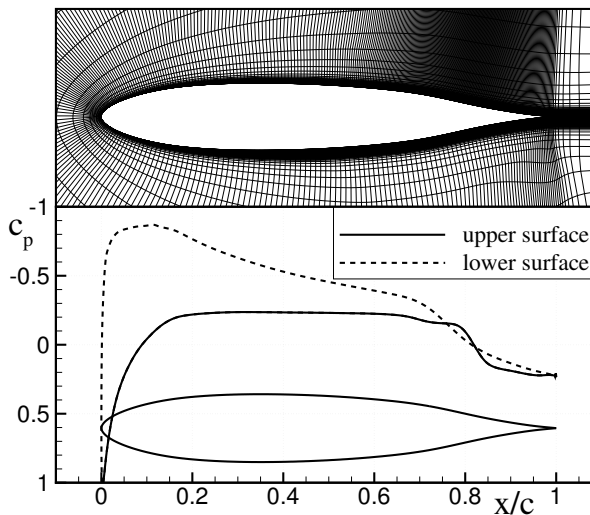


Fig. 7: Standard computational grid for XIS40MOD airfoil and computed distribution of pressure coefficient at $Re = 1.2 \cdot 10^6$, $\alpha = -3^\circ$

compared with the one-equation model of Spalart and Allmaras, two variants of the $k - \omega$ model and the SSG Reynolds-stress model in **Fig. 10** and **11**. Note that different numerical transitions locations were used as the individual models predict a rather different rise of turbulence and turbulent eddy viscosity downstream of the nominal transition location. For example, it appears that the growth of turbulent kinetic energy predicted by the original $k - \omega$ model is rather slow, compared to the others. Therefore, in order to compute similar positions of the turbulent reattachment for this model one has to specify the nominal transition position significantly upstream. The results indicate that the differential-equation turbulence models predict a too slow growth of turbulence in the separation bubble. Accordingly, the rise of wall shear stress in the re-attachment region is much too slow either. This problem is more striking for the original $k - \omega$ model whereas the Spalart-Allmaras, the SST and the SSG models perform somewhat better. Note that the SST model uses the $k - \varepsilon$ formulation far away from walls and this seems to be the reason for the more rapid growth of turbulence compared to the $k - \omega$ model. This holds true for the SSG model as well. The algebraic Baldwin-Lomax model, on the other hand, yields an instantaneous switch to fully turbulent flow right at the nominal transition point. It turns out that this results in rather close agreement of the predicted pressure distribution. However, all models share the unsatisfactory result that the wall shear stress is significantly underpredicted downstream of re-attachment. Here, the high complexity of the Reynolds-stress model seems have a positive effect, as it predicts the highest level of turbulent shear stress of all models. However, the results of the currently implemented Reynolds-stress model can only be understood as step in the right direction. Please note that the experimental hot-wire set up could not measure reverse flow. Therefore, the positive, experimental values of c_f within the separated flow region are false.

The flow structures of the laminar separation bubble predicted by the algebraic model and the SST model are displayed in **Fig. 12**. The vertical co-ordinate is enlarged by a factor of 3 in order to make the differences visible. The SST model predicts a shallow shape of the separation bubble whereas the bubble of the algebraic model closes much more rapidly. A fast turning vortex is created in the aft part of the LSB by the sudden onset of turbulent viscosity with the Baldwin-Lomax model. This vortex corresponds to a local peak in the boundary-layer edge velocity at $x/c = 0.8$, which is visible in both, computation and experiment.

Next, the effect of grid density on the predicted N-factor is investigated. **Figure 13** displays the N-factor distribution that results either from using the approximate envelope method or from solving the local linear stability equations with the Coast3 code. Coast3 is used in two ways: In one way only the pressure distribution from FLOWer is used, and the affiliated boundary layer method “Coco” generates the velocity and temperature profiles up to the point of separation. In the other way, the profiles are used directly from the

RANS Simulation of the Transitional Flow Around Airfoils at Low Reynolds Numbers for Steady and Unsteady Onset Conditions

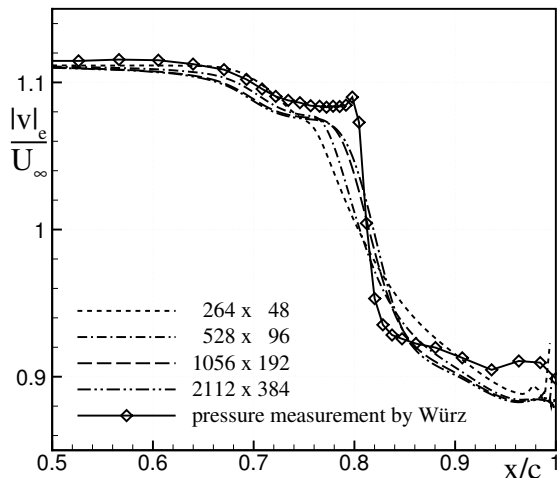


Fig. 8: Boundary layer edge velocity for different grid densities

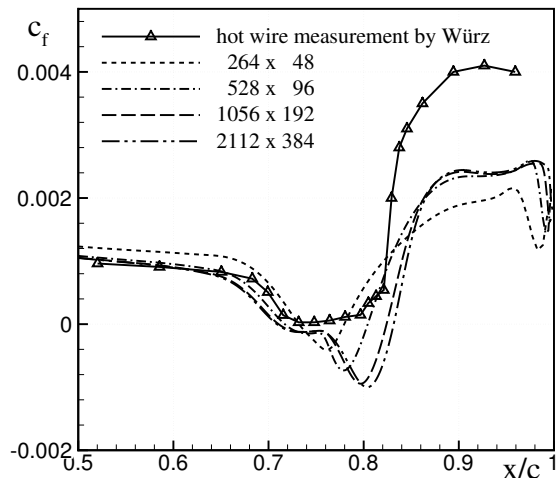


Fig. 9: Coefficient of wall shear stress for different grid densities

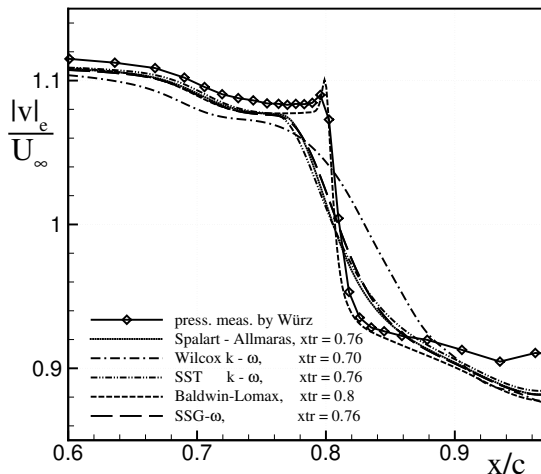


Fig. 10: Boundary layer edge velocity for different turbulence models

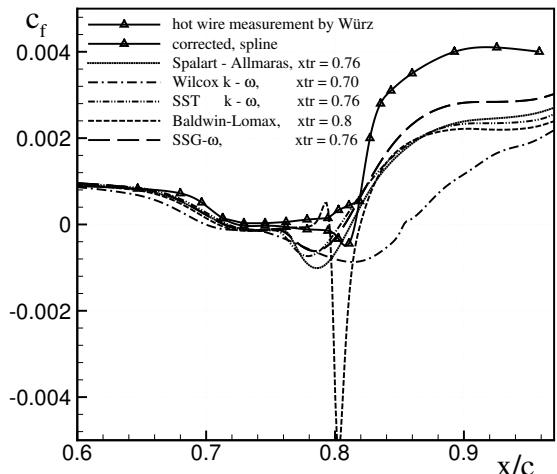


Fig. 11: Coefficient of wall shear stress for different turbulence models

Navier-Stokes method over the whole airfoil. As the accuracy of the laminar mean flow improves on finer meshes one observes a small rise of N -values with an increasing number of points in the boundary layer. For about 70 points in the boundary layer good agreement with the measurement as well as the N -factor distribution based on the pressure distribution is found. The approximative envelope method also shows quite good agreement in the region of attached flow. The increasing disagreement above the LSB is due to the fact that the method assumes Hartree-profiles (see 2.1.3), which is invalid in the region of the LSB.

Finally, the iterative convergence of transition location with time is displayed in Fig. 14. The computation was started from an initial transition location close to the trailing edge. This provokes laminar flow separation in the initial phases of the computation. The separation then grows until the N -factor becomes larger than the critical value. Then, transition jumps upstream and re-attachment is obtained by turbulent momentum transport. Finally, the transition location converges continuously to the steady-state result. This takes about 300 physical time steps of $\Delta t = 0.01$, according to Fig. 14. In conclusion we notice that the computations of the XIS40MOD airfoil display a strong sensitivity of the computed LSB to spatial discretisation errors. However, extraction of sufficiently accurate boundary layer data for transition prediction is feasible. The major problem in physical modelling of this case seems to be the turbulence model. Two-equation models

RANS Simulation of the Transitional Flow Around Airfoils at Low Reynolds Numbers for Steady and Unsteady Onset Conditions

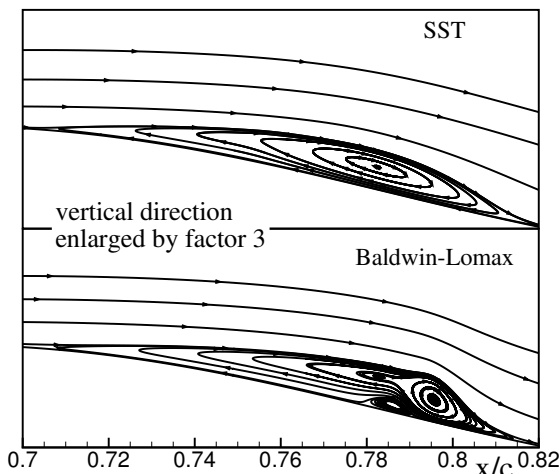


Fig. 12: Comparison of flow streamlines for two turbulence models

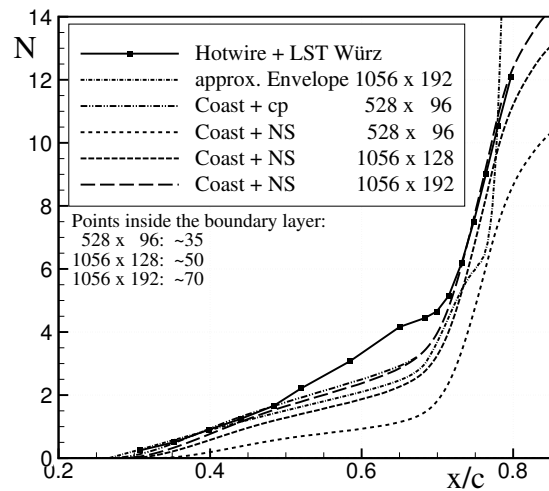


Fig. 13: Sensitivity of the N-factor distribution on methods and grid density, SST-model with $x_{tran} = 0.76$

do not predict the strong rise of shear stress that would bring the pressure distribution and wall shear stress close to the experimental observations. The good agreement of the algebraic model in terms of pressure distribution seems fortuitous as this model simply neglects any history effects of turbulence associated with convection and diffusion.

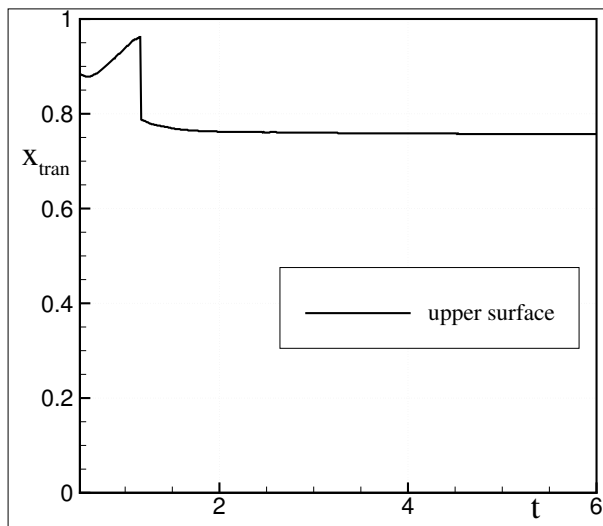


Fig. 14: Iterative convergence of transition location with SST-model

5.1.2 Flow Computations of SD7003 Airfoil

The SD7003 airfoil is designed for model airplanes that operate in the Reynolds number range of $0.5 \cdot 10^5 - 2 \cdot 10^5$. The pressure distribution exhibits a carefully controlled adverse pressure gradient ahead of laminar separation. This strategy yields growing disturbances ahead of the separation. Furthermore, the adverse pressure gradient in the rear of the airfoil is rather limited, due to the small airfoil thickness of around 8 percent and its forward location of the point of maximum thickness. The resulting separation bubble is therefore thin over the full angle of attack range, even for Reynolds numbers below 10^5 . Hence, the airfoil is not suspect to the break up of the laminar separation bubble within its design range and it is a good test case to assess

RANS Simulation of the Transitional Flow Around Airfoils at Low Reynolds Numbers for Steady and Unsteady Onset Conditions

computational capabilities.

Recently, 2D phase locked PIV measurements were conducted on the upper side of the SD7003 in a low turbulence ($Tu = 0.0012$) windtunnel (LNB) at Braunschweig Technical University. The wing section with chord length 200mm and span 400mm was made out of glass fibre reinforced plastics and fitted in the 400mm \times 600mm \times 1200mm test section of the windtunnel. The measurements were carried out at an angle of attack of $\alpha = 4^\circ$ and a Reynolds number of $Re = 60000$ with the commercial PIV system Flow Master 3S and a frequency doubled Quantel Twin double pulsed Nd:YAG-laser. To achieve highly detailed measurements along the upper side, the observation domain was translated to 9 different positions, each with a field of view of 27.27mm \times 21.81mm. At each of the 9 locations 1000 statistically independent PIV images were recorded in order to calculate the mean velocity and three components of the Reynolds stress tensor. For the evaluation of all images the commercial PIV software DaVis 6.2 was used. Because of a high seeding density it was possible to choose small interrogation windows with a size of 16px \times 16px. Together with an overlap of 50 percent a spatial resolution of 0.17mm could be achieved. The absolute particle image displacement range was determined to be between 0.004px and 14.36px which is in an appropriate range for small measurement errors.

The computational standard mesh for the numerical investigation of the SD7003 airfoil contains 528x96 cells, as for the previous case. Grid convergence studies using a coarse 264x48 mesh in addition indicate that this case is, because of the now lower Reynolds number, less sensitive to grid density as the XIS40MOD airfoil. This is displayed for the flow at a moderate angle of attack by using the SST turbulence model in **Fig. 15**. The distribution of wall-shear-stress coefficient indicates that a mesh with 528x96 cells is sufficient for LSB computations at low Reynolds numbers. The non-dimensional time step was chosen as $\Delta t = 0.01$ and around 1000 time steps were needed for convergence. Note that the number of inner iterations in the dual time stepping method was around 20. Typical pressure distributions for a variety of angles of attack are displayed in **Fig. 16**. The LSBs are seen as local plateaus. The lower surface is fully laminar for all angles larger than zero. The LSB moves from the trailing edge to the leading edge as the angle of attack is increased.

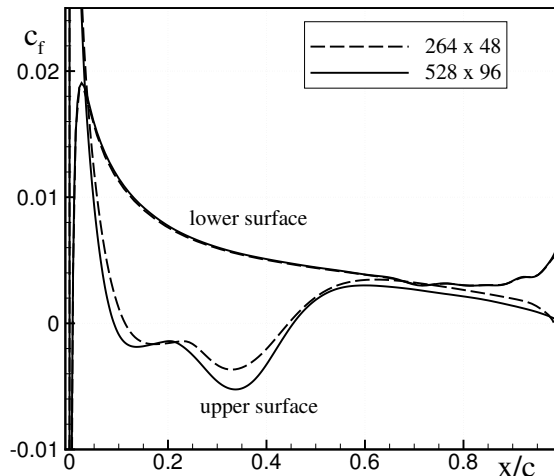


Fig. 15: Grid convergence of wall shear stress for $\alpha = 6^\circ$, SST-model

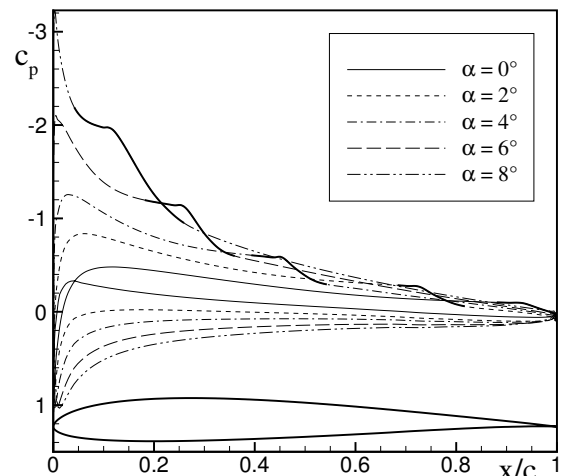
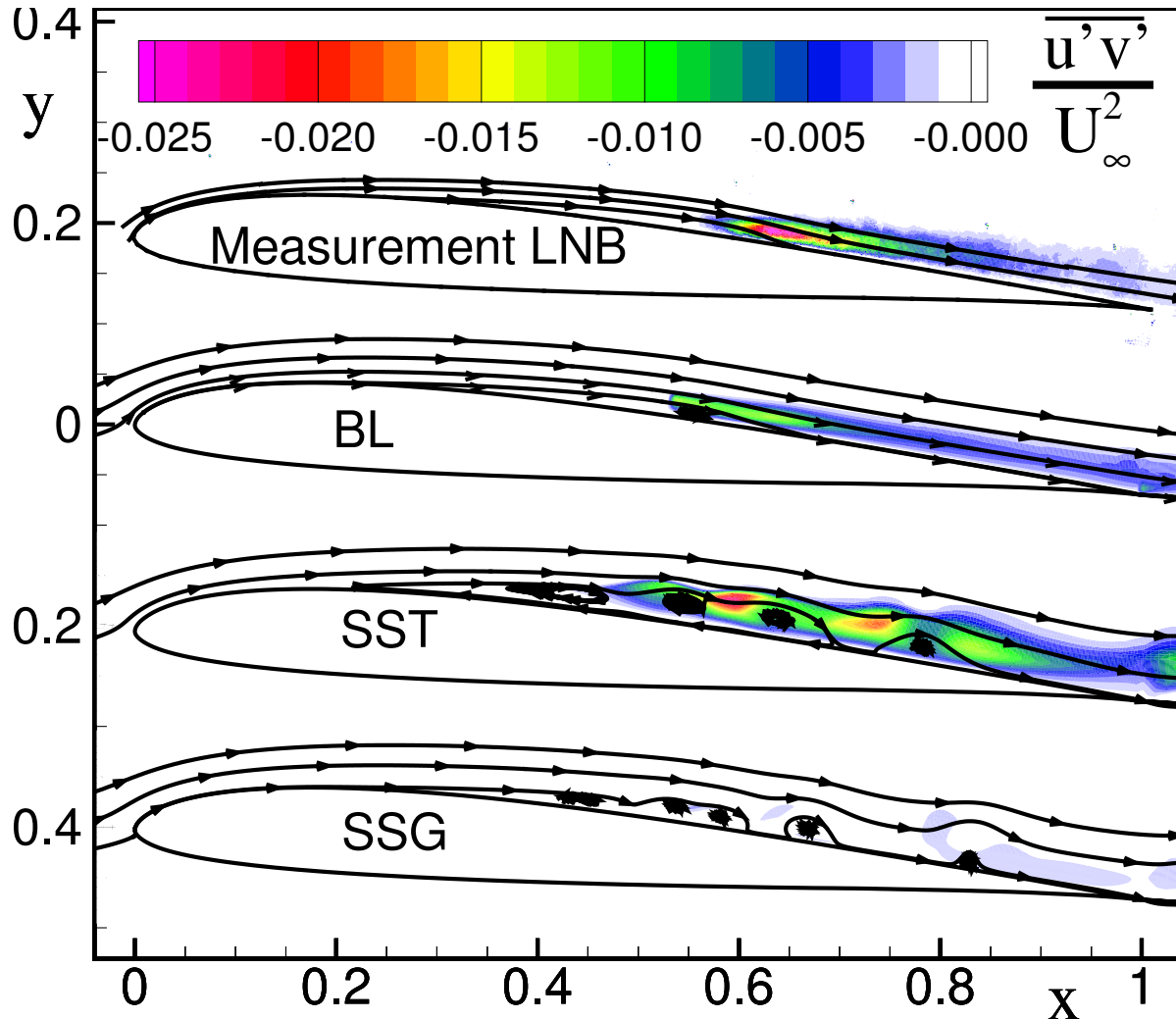


Fig. 16: Computed pressure distributions with the Baldwin-Lomax model

Figure 17 compares the turbulent shear stress from the PIV measurement at $\alpha = 4^\circ$ with the computations for different turbulent models, using the coupled linear stability solver coast3. The transition location in the measurement is found extrapolating the wedge that is formed by the turbulent shear stress into the upstream direction. The so found transition location lies at about the thickest point of the LSB, as the effect of the turbulence is the closure of the bubble, and can be given to about $x_{tran,meas.} = 0.56$. From that point on the turbulent shear stress continuously grows up to a maximum dimensionless value of -0.026,


 Fig. 17: Measured and computed turbulent shear stress at $\alpha = 4^\circ$

which is reached about 9.5 percent of the chord length c downstream. Using a critical N-factor of $N_{crit} = 8$ which fits the turbulence level of the windtunnel according to Mack's relation from chapter 2.1.2 and the algebraic Baldwin-Lomax (BL) turbulence model, the transition location is computed at $x_{tran,BL} = 0.53$. As the Baldwin-Lomax model produces large amounts of turbulence instantaneously at the transition point, the bubble is closed at about the same point as in the measurement, even though only a nondimensional shear stress of about half the measured value is reached. The fact that the transition location was calculated a few percent upstream of the measured indicates that the N-Factor was chosen slightly to small, but this results in a good overall simulation with the BL-model. With the SST-model, a transition location of $x_{tran,SST} = 0.42$ is found, while the first maximum of the nondimensional shear stress (for the shown instantaneous flow state) is reached 10.5 percent of c downstream of that. Although the unsteady flow behavior given by the SST-model appears much closer to the experimental findings compared to the BL-model, the produced turbulent shear stress is (at the first maximum) again only half of the measured value. As this is not sufficient to close the bubble, it becomes larger compared to the BL-model and sheds vortices at its end. Because the thicker upstream region of the bubble yields larger amplifications of disturbances, the transition location is computed 11 percent upstream compared to the BL-model. The SSG-model experiences the same problems as the SST-model, but even more pronounced. Note that this model shows the best overall performance at higher Reynolds numbers [19] and was still the superior transport equation turbulence model at the previous

RANS Simulation of the Transitional Flow Around Airfoils at Low Reynolds Numbers for Steady and Unsteady Onset Conditions

case at an already low Reynolds number of $Re = 1.2E6$. It can be concluded that the algebraic BL-model is best suited for the simulation of this case, despite its unphysical behaviour. Large improvements could be expected from a model based on transport equations which would be able to predict the strong rise of the turbulent shear stress behind the LSB.

5.2 Unsteady Onset Conditions

5.2.1 Flow Computations of SD7003 Airfoil

To validate the later described numerical results measurements were conducted in the watertunnel at Braunschweig Technical University. The facility has a free stream turbulence level of $Tu = 0.01$, which translates into a critical N-factor of $N_{crit} = 2$ using eq. 13. The SD7003 wing section with 200mm chord length and a span of 248mm was mounted on a plunging mechanism, as described in [23]. The mean angle of attack was set to $\alpha_0 = 5.5^\circ$. A Reynolds number of $Re = 60000$ resulted from the onset velocity at infinity of $U_\infty = 0.3m/s$ and a water temperature of 20° . As a flapping frequency of $f = 0.25Hz$ and a plunging amplitude of $z_1 = 10mm$ were used, the resulting quasisteady equivalent angle of attack amplitude from plunging can be calculated to $\zeta_1 = \frac{2\pi f z_1}{U_\infty} = 3^\circ$. The resulting effective angle of attack for the airfoil motion then reads $\alpha_{eff} = \alpha_0 + \zeta_1 \sin(2\pi f t) = 5.5^\circ + 3^\circ \sin(2\pi f t)$. The airfoil was driven by an eccentric mechanism with 1 percent derivation to the ideal sinusoidal stroke. Almost the same 2D PIV set up was used as for the windtunnel measurements described above. The field of view was only slightly bigger ($31.24mm \times 24.99mm$), which led to a spatial resolution of $0.2mm$. To cover most of the separation bubble, two slightly overlapping locations of 30mm distance were chosen. Phase locked measurements were performed for the four motion positions top dead centre (TDC) ($\alpha_{eff} = 5.5^\circ$), downstroke ($\alpha_{eff} = 8.5^\circ$), bottom dead centre (BDC) ($\alpha_{eff} = 5.5^\circ$) and upstroke ($\alpha_{eff} = 2.5^\circ$). Additional measurements were carried out for these four angles of attack for steady onset conditions.

The following numerical results were obtained using the e^N -method with the extension for unsteady flows as described in chapter 2.1. A first verification of the method was achieved by a calculation of a case with steady onset condition, first with the steady N-Factor integration schema and second, as a restart, with the unsteady one. There, the obtained N-Factor distribution converged to a steady state solution that agreed within plotting accuracy.

As the BL turbulence-model showed the best performance for the steady onset condition calculations in the previous case, it was chosen for the first unsteady calculation, which is presented in the following. To take into account the wall effect from the above watertunnel experiment, a simple wall correction for steady flows from [24] was applied. This results into an effective angle of attack of $\alpha_{eff} = 6^\circ + 3.3^\circ \sin(2\pi f t)$ which was used for the calculations. As the calculation has to be done for nondimensional values, a reduced frequency of $k = \pi f c / U_\infty = 0.52$ and a plunge amplitude of $z_1 / c = 0.0554$ were used. The used computational mesh is similar to the previous case and has a density of 472x96 points.

Figure 18 shows the obtained temporal distribution of transition location and lift coefficient, using a coarser mesh of only 236x48 points for the first three motion periods. The nondimensional timestep was chosen ten times too large with $\Delta t = 0.085$ during the first five motion periods, which led to some small oscillations in the transition location during the fourth and fifth motion period. The sixth and seventh motion periods were then calculated using 2000 timesteps with $\Delta t = 0.0085$ each. As no significant differences are found between the end of the sixth and seventh period, a periodic solution is found for the seventh motion period.

Figure 20 shows the turbulent shear stress $\overline{u'v'}$ obtained by a phase locked measurement during the downstroke of the airfoil. Even after averaging over 1000 frames there are regions found with elevated shear stress, which represent vortices shed at the end of the LSB. This indicates that the periodic shedding of vortices behind the LSB is coupled to the plunge motion, which has a much lower frequency. The transition locations for these phase locked measurements have been determined similar to the measurement at steady onset conditions in the windtunnel described earlier. Here, as a LSB with shed vortices has been measured, the first local maximum of the bubble corresponds to the transition location according to the onset of the turbulent

RANS Simulation of the Transitional Flow Around Airfoils at Low Reynolds Numbers for Steady and Unsteady Onset Conditions

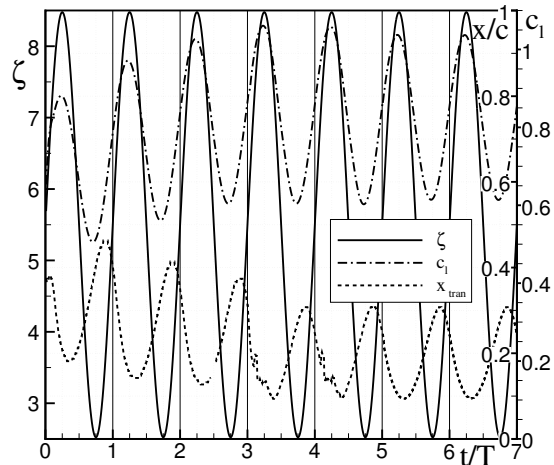


Fig. 18: Temporal distribution of transition location and lift coefficient

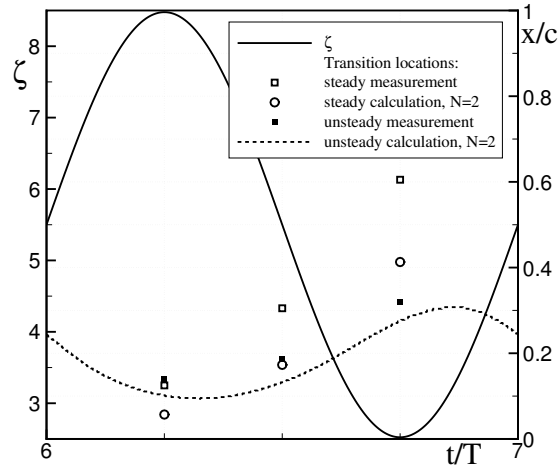


Fig. 19: Comparison of measured and calculated transition locations

shear stress.

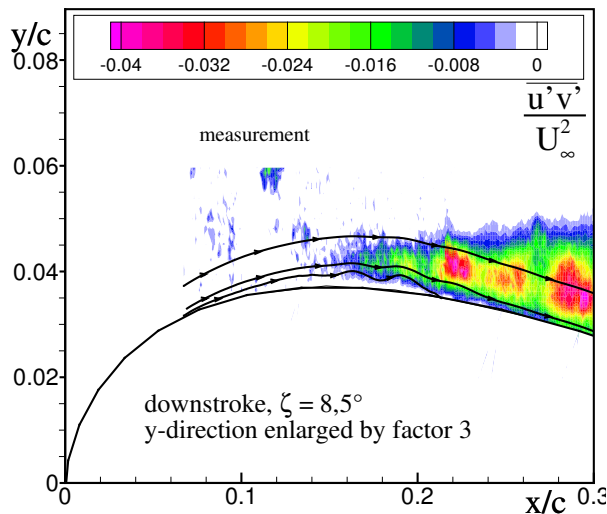


Fig. 20: Measured turbulent shear stress during downstroke

The transition locations found in the computations, in the phase locked measurements and in the steady state flow measurements with the quasisteady equivalent angles of attack are shown in **Fig. 19**. The comparison between the measurements and computations for steady onset conditions show a large discrepancy between the transition locations. It can be concluded that either the water tunnels turbulence level is less than measured, or the correlation of Mack is not working properly for the quite high turbulence level of $Tu = 0.01$ of the watertunnel. For the unsteady computation, the too low chosen N-factor of $N = 2$ again results in a transition location upstream of the measurement, but now with a smaller and about constant distance. It is interesting to see here that the unsteady transition locations (calculation and measurement) are downstream of the steady ones at $\zeta = 8.5^\circ$, while it is the other way around at the lower angles. This behaviour still needs to be explained. The computed unsteady transition location shows a phase shift of 25° during the downstroke and 40° during upstroke, which is about the expected effect at the examined reduced frequency of $k = 0.52$. The lift coefficient however seems to be more dependant on the mean flow and does not show much phase shift, as seen in **Fig. 18**.

The measured and computed LSBs are finally compared at the dead centres, downstroke and upstroke

RANS Simulation of the Transitional Flow Around Airfoils at Low Reynolds Numbers for Steady and Unsteady Onset Conditions

in **Fig. 21**, together with the nondimensional total velocity $\vec{U} = \sqrt{U^2 + V^2}$. In order to be able to draw streamlines, the v -component of the velocity was corrected with the plunging velocity of the airfoil, leading to a velocity of zero on the surface of the airfoil. It can be seen that despite the same quasisteady angle of attack of $\zeta = 5.5^\circ$, there are completely different flow states found at TDC and BDC. While the LSB that formed during the downstroke is clearly visible at BDC, it is vanishing during upstroke and can hardly be seen at all at TDC. A transition location can not be determined in the measurement for TDC. During downstroke, the calculated LSB is clearly higher than the measured one. Correspondingly, the point of laminar separation $x_{sep}/c = 0.05$ is situated a little ahead of the measured one at $x_{sep}/c = 0.065$. At BDC a vortex is shed from the LSB in the simulation, which leads to about the same thickness of the LSB in the front part as in the measurement. The point of laminar separation is again somewhat ahead in the calculation.

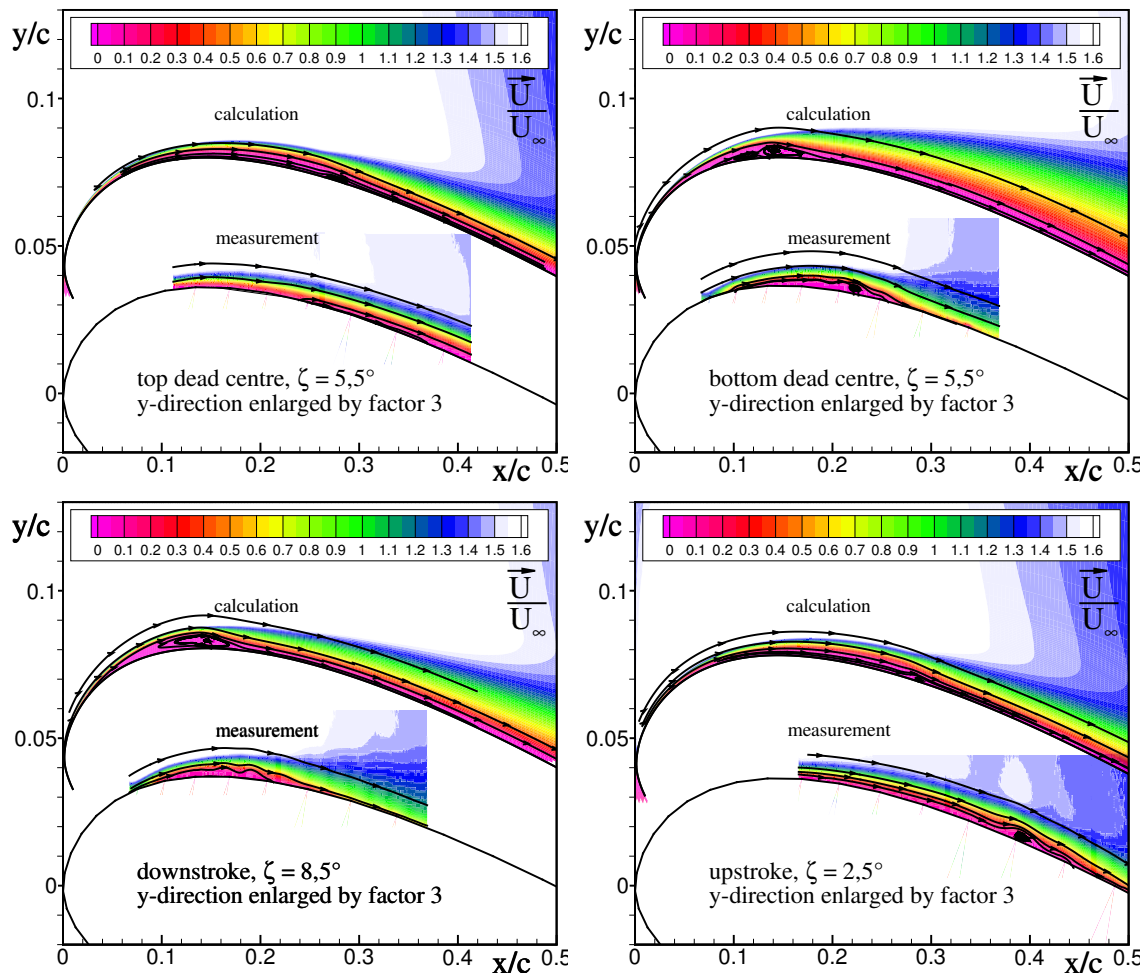


Fig. 21: Comparison of streamlines and velocities between measurement and calculation at four different times

6 SUMMARY

Transitional flows around airfoils were calculated for steady as well as unsteady onset conditions using a Reynolds-averaged Navier-Stokes method. Hereby, the transition location was found using the e^N -method in combination with a linear stability solver. In order to do so, a new temporal integration schema for the e^N -method was used. It was pointed out that the N-Factor distribution needs special treatment in the vicinity of the transition location, i.e. extrapolation.

For the flows with steady onset conditions it was shown that high grid densities are necessary to obtain



RANS Simulation of the Transitional Flow Around Airfoils at Low Reynolds Numbers for Steady and Unsteady Onset Conditions

grid convergence. It was shown that the main remaining sensitivity for the flows with LSB is the turbulence model, and that further improvement in that field is needed.

A first solution was presented for the transitional flow around a moving airfoil using the new temporal schema. It was found for the investigated case that very different flows form at the quasisteady identical angles of attack at the dead centres, thus the flow has an unsteady character. The computed unsteady transition locations were promising compared to the measurement.

ACKNOWLEDGEMENT

The present research was partly funded by the “Deutsche Forschungsgemeinschaft (DFG)”. Also, the authors thank Mr. Schrauf for providing the linear stability solver “Coast3”.

REFERENCES

- [1] F.W. Schmitz: “Aerodynamik des Flugzeugs”. Verlag Carl Lange, Duisburg, 1960.
- [2] R. Eppler: “Airfoil Design and Data”. Springer Verlag, ISBN 3-540-52505-X, 1990.
- [3] D. Althaus: “Profilpolaren für den Modellflug”. Neckar Verlag Villingen, Bd. I: ISBN 3-7883-0158-9, 1980; Bd. II: ISBN 3-7883-0134-1, 1985.
- [4] M.S. Selig, J.F. Donovan, D.B. Fraser: “Airfoils at low speeds”. SoarTech 8, SoarTech Publications, H.A. Stokely, Virginia Beach, VA, USA, 1989.
- [5] M.S. Selig et al: “Summary of low-speed airfoil data” Vol. 1-3, SoarTech Publications, H.A. Stokely, Virginia Beach, VA, USA, 1995, 1996, 1997.
- [6] W. Würz: “Hitzdrahtmessungen zum laminar-turbulenten Strömungsumschlag in anliegenden Grenzschichten und Ablöseblasen sowie Vergleich mit der laminaren Stabilitätstheorie und empirischen Umschlagskriterien”. Dissertation an der Universität Stuttgart, 1995.
- [7] M. Lang, O. Marxen, U. Rist, S. Wagner: “Experimental and numerical investigations on transition in a laminar separation bubble”. In: S. Wagner, U. Rist, H.J. Heinemann, R. Hilbig (eds.): New Results in Numerical and Experimental Fluid Mechanics III, Proc. 12. DGLR-Fachsymposium AG STAB, Stuttgart, Nov. 2000, NNFM Vol.77, Springer Verlag, 2001.
- [8] O. Marxen, U. Rist, S. Wagner: “The effect of spanwise-modulated disturbances on transition in a 2-d separated boundary layer”. AIAA Paper 2003-0789, 2003.
- [9] M. Drela: “XFOIL: An analysis and design system for low Reynolds number airfoils”. In T.J. Mueller: Low Reynolds number aerodynamics, Lecture Notes in Engineering, Springer Verlag, New York, 1989.
- [10] U. Rist: “Zur Instabilität und Transition in laminaren Ablöseblasen”. Habilitation an der Universität Stuttgart, Shaker Verlag, Aachen, 1999.
- [11] J.H. Watmuff: “Evolution of a wave packet into vortex loops in a laminar separation bubble”. J. Fluid Mech., Vol. 397, 1999, pp.119-169.
- [12] D. Arnal: “Description and prediction of transition in two-dimensional, incompressible flow”. AGARD R 709, 1984.
- [13] L.M. Mack: “Transition and laminar instability”. Jet Propulsion Laboratory Publication 77-15, Pasadena, 1977.
- [14] B.S. Baldwin, H. Lomax: “Thin-layer approximation and algebraic model for separated turbulent flows”. AIAA Paper No. 78-257, 1978.

- [15] P.R. Spalart, S.R. Allmaras: "A one-equation turbulence model for aerodynamic flows". AIAA Paper 92-439, 1992.
- [16] F.R. Menter: "Two-equation eddy-viscosity transport turbulence model for engineering applications". AIAA Journal, Vol. 32, 1994, pp. 1598-1605.
- [17] C. G. Speziale, S., Sarkar, T. B. Gatski: "Modelling the pressure-strain correlation of turbulence: an invariant dynamical systems approach". J. Fluid Mech. **227**, 1991, pp. 245-272
- [18] D.C. Wilcox: "Turbulence modelling for CFD". Second edition, DCW Industries, La Canada, Ca, ISBN 0-9636051-5-1, 2000.
- [19] B. Eisfeld: "Numerical simulation of aerodynamic problems with Reynolds stress turbulence models". Contribution to the 14th DGLR/STAB Symposium, 2004, to appear
- [20] N. Kroll, C.C. Rossow, D. Schwamborn, K. Becker, G. Heller: "MEGAFLOW - A numerical flow simulation tool for transport aircraft design". Proceedings ICAS 2002 Congress, Paper No. 1105, 2002.
- [21] G. Schrauf: "Coast3 - A compressible stability code. User's guide and tutorial". Daimler-Benz Aerospace Airbus GmbH, Technical Report EF 040/98, Bremen, Germany, 1998.
- [22] G. Schrauf: "An inverse Rayleigh iteration for complex band matrices". ALGORITHM 696, ACM TOMS, Vol. 17, 1991, pp. 335-340.
- [23] D. Nerger, C.J. Kähler, R. Radespiel: "Zeitaufgelöste PIV-Messungen an einem schwingenden SD7003-Profil bei $Re=60000$ ". Lasermethoden in der Strömungsmesstechnik, 11. GALA Fachtagung, 9.-11. September, Braunschweig, 2003.
- [24] AGARD-AG-336: "Wind Tunnel Wall Corrections". October 1998.